PHYSICAL REVIEW B **79**, 035420 (2009)

Structural and vibrational properties of two-dimensional Mn_xO_y layers on Pd(100): Experiments and density functional theory calculations

C. Franchini*
Faculty of Physics, Center for Computational Materials Science and Universität Wien, A-1090 Wien, Austria

R. Podloucky
Institut für Physikalische Chemie, Center for Computational Materials Science and Universität Wien, A-1090 Wien, Austria

F. Allegretti,† F. Li, G. Parteder, S. Surnev, and F. P. Netzer
Institute of Physics, Surface and Interface Physics, Karl-Franzens University Graz, A-8010 Graz, Austria
(Received 16 October 2008; revised manuscript received 28 November 2008; published 29 January 2009)

Using different experimental techniques combined with density functional based theoretical methods we have explored the formation of interface-stabilized manganese oxide structures grown on Pd(100) at (sub-)monolayer coverage. Among the multitude of phases experimentally observed we focus our attention on four structures which can be classified into two distinct regimes, characterized by different building blocks. Two oxygen-rich phases are described in terms of MnO(111)-like O-Mn-O trilayers, whereas the other two have a lower oxygen content and are based on a MnO(100)-like monolayer structure. The excellent agreement between calculated and experimental scanning tunneling microscopy images and vibrational electron-energy-loss spectra allows for a detailed atomic description of the explored models.

DOI: 10.1103/PhysRevB.79.035420 PACS number(s): 68.47.Gh, 68.37.Ef, 61.05.jh, 68.43.Bc

I. INTRODUCTION

Ultrathin oxide films grown on metal surfaces with thicknesses in the nanometer range are promising systems, where the reduced dimensionality and the dominance of surface and interface effects may lead to novel physical and chemical properties, intrinsically different from those of the corresponding bulk counterparts. As such, low-dimensional oxide films with tailored properties are increasingly exploited in technological applications, as for example in micro- and nanoelectronics, magnetic recording, and heterogeneous catalysis.

From a structural point of view, systems only a few atomic layers thick are often different from the bulklike phases in terms of local coordination, long-range ordering, and surface symmetry. As a consequence of the interaction with the support, even terminations which are not favored as bulk-truncated surfaces may be stabilized, and depending on the growth conditions several different structures appear.

For 3*d* transition-metal oxides, numerous structural studies of interfacial phases on various substrates are available in the literature, such as FeO on Pt(111),[1,2] Pt(100) (Ref. 3) and Ru(0001),[4] vanadia on Pd(111) (Refs. 5–7) and Rh(111),[8–10] Ni oxide on Pd(100) (Refs. 11 and 12) and Ag(100),[13,14] CoO(111) on Ir(100) (Ref. 15), and Mn oxide on Pt(111).[16] In the present study we focus on the Mn oxide phases formed at a Mn coverage of up to 1 monolayer (ML) on Pd(100). We have previously characterized the high thickness regime (15–20 ML), showing that MnO(100) with bulklike in-plane lattice constant is stable in a wide range of pressure and temperature;[17] however, at more reducing conditions MnO with (111) orientation can be grown. The MnO(111) surface is polar, and at high thickness the films tend to become unstable toward faceting: as a result, the morphology is dominated by triangular pyramids exposing the lowest-energy (100) facets.[17] At the other extreme of oxidizing conditions, we have demonstrated that flat MnO(100) films can be preferentially oxidized to yield Mn_3O_4(001) (Ref. 18).

Below 1 ML, a complex phase diagram of Mn oxides on Pd(100) is observed[19] composed of nine different interface-stabilized phases. The experimental phase stability diagram as a function of the oxygen pressure $P(O_2)$ and of the O chemical potential μ_O is depicted schematically in Fig. 1. It comprises: (i) two hexagonal phases (HEX-I and HEX-II), which are both obtained at high O_2 pressures (above 5×10^{-7} mbar); (ii) a $c(4\times2)$ structure and a *stripe* phase described as a uniaxially compressed $c(4\times2)$, which are both stabilized at intermediate O_2 pressures (around 5×10^{-7} mbar); (iii) two structures which were called *chevrons* (CHEV-I and CHEV-II) because of their STM appearance; (iv) two reduced phases with complex structures named *waves* and *labyrinth*; (v) finally, at the most reducing conditions, a third hexagonal phase (HEX-III), commensurate with the Pd(100) substrate ($\times2$) along one of the two $\langle011\rangle$ directions.

Here, we aim to rationalize this extraordinary architectural flexibility of the interfacial Mn oxides on Pd(100) in terms of realistic structural models. On the basis of high-resolution electron-energy-loss spectroscopy (HREELS) data we show that it is possible to distinguish two different oxygen regimes: an O-rich regime comprising the HEX-I and HEX-II phases and characterized by a dominant phonon loss at ≈70 meV, and an O-poor regime encompassing all other phases, which display a single phonon loss at ≈44 meV. Theoretical models based on an educated guess of possible structures are tested and directly compared with scanning tunneling microscopy (STM), low-energy electron diffraction (LEED), and HREELS results. In the following, we consider in detail four phases, $c(4\times2)$, CHEV-I, HEX-I, and HEX-II, for which the atomic scale modeling represents a

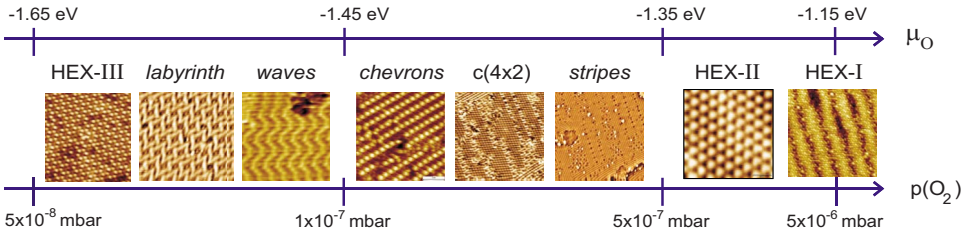

FIG. 1. (Color online) Experimental schematic phase stability diagram of the interfacial Mn oxides presented as a function of the oxygen pressure $P(O_2)$ and of the oxygen chemical potential μ_O (Ref. 19). The nominal coverage of Mn on Pd(100) is ~0.75 ML.

computationally affordable task due to the relatively small size of the surface unit cell. Through the combined theoretical and experimental investigation, it is concluded that the two O-rich phases can be described in terms of O-Mn-O trilayers with a MnO(111)-like structure, whereas the O-poor regime is based on a compressed MnO(100)-like model. We find that the high degree of flexibility of these two basic models is favored by the formation of regular arrays of vacancies, in line with previous investigations on related systems.[12,16] Importantly, our description provides a natural link between the interfacial phases and the MnO(100) and MnO(111) films of the high thickness regime.

The paper is organized as follows: the experimental procedures and computational details are described in Secs. II A and II B, respectively. In Sec. III A we discuss the main experimental evidence for the existence of two different oxygen pressure regimes; full structural models for the $c(4\times2)$ and CHEV-I of the O-poor or intermediate-O regime are presented in Sec. III B, while the proposed atomic structure for the HEX-I and HEX-II phases of the O-rich regime is discussed in Sec. III C. Finally, Sec. IV is devoted to the summary and conclusions.

II. TECHNICAL ASPECTS

A. Experimental procedure

The experiments have been conducted in a number of different ultrahigh vacuum (UHV) chambers with typical base pressure $p=1-2\times10^{-10}$ mbar. The structure and morphology of the Mn oxide films were characterized by STM measurements performed in our home laboratories in Graz, in two different custom-designed systems. One STM system comprises a variable-temperature STM (Oxford Instruments), a LEED optics, a cylindrical mirror analyzer for Auger electron spectroscopy, and the usual facilities for crystal cleaning and physical vapor deposition. The other STM system is equipped with a variable-temperature AFM-STM Omicron apparatus and a LEED optics. All STM images were recorded in constant current mode at room temperature (300 K) with electrochemically etched W tips, which were cleaned *in situ* by electron bombardment. These measurements were complemented by spot-profile analysis low-energy electron diffraction (SPA-LEED) experiments performed in an independent UHV chamber, which has been described in more detail elsewhere.[20] HREELS measurements were performed to elucidate the phonon structure of the oxide layers, using an ErEELS (Erlangen EELS) spectrometer,[21] which was operated in specular reflection geometry at 60° incidence from the surface normal and with a primary energy of 6.5 eV. The crystal was kept at room temperature (RT) during the measurements, and a typical resolution of 6 meV was ensured, as measured at the full width at half maximum of the reflected primary peak. LEED provided a common link with the structures prepared in the various chambers.

The clean Pd(100) crystal surface was prepared by the usual combination of 1 keV Ar^+-ion sputtering and annealing at 1000 K. Further annealing for 3–5 min in O_2 atmosphere (2×10^{-7} mbar) at 570 K, followed by a brief flash to 1000 K in UHV, was used to remove contamination of residual atomic carbon. The preparation protocol for the interfacial manganese oxide layers on Pd(100) consists of deposition of Mn metal in UHV with the sample kept at RT, followed by postoxidation (PO) at higher temperature in a molecular oxygen atmosphere. This PO procedure has been preferred over the reactive evaporation (RE) procedure involving deposition of Mn in oxygen atmosphere, because it typically provides films with smoother morphology and containing a single dominant phase, as judged by STM and LEED.[19] The Mn deposition rate was monitored by a quartz crystal microbalance, and evaporation rates of 0.5 ML min^{-1} or less were usually employed, with 1 ML containing 1.32×10^{15} Mn atoms/cm^2 as referred to the Pd(100) surface atom density. O_2 pressures in the range 1×10^{-7}–5×10^{-6} mbar (Ref. 22) and sample temperatures in the range 600–700 K were used, the exact combination of these parameters crucially depending on the desired long-range-ordered phase.

Of the four different phases considered in detail in this work, the HEX-I phase is obtained by postoxidation of 0.75 ML Mn at 670 K at the highest oxygen pressure employed (5×10^{-6} mbar O_2), while the CHEV-I structure is typically prepared by postoxidizing the same amount of Mn at 700 K and low O_2 pressure (1×10^{-7} mbar). Transition between these two phases, and also to the other intermediate phases $c(4\times2)$ and HEX-II, is made possible by annealing the HEX-I phase in UHV or low O_2 pressure at 650–700 K, or by performing a second postoxidation of the CHEV-I phase at increasing O_2 pressure.

B. Computational details

The present calculations were carried out using the projector augmented wave (PAW) (Refs. 23 and 24) based Vienna *ab initio* simulation package (VASP) (Ref. 25) in the framework of standard (Kohn-Sham theory) and generalized (hybrid) density functional theory (DFT). The choice of adopting a method beyond standard DFT is due to the complex nature of the system to be described. Although the metallic character of the Pd support is correctly described within DFT, this is not true for the correlated nature of the

magnetic Mn_xO_y overlayers. In a series of recent papers[17,26–28] we have provided a detailed description of the obstacles that standard DFT faces when applied to manganese oxides. We have shown that the application of methods beyond DFT such as HSE (Heyd-Scuseria-Ernzerhof) is essential to correct the self-energy related DFT drawbacks and to provide a satisfactory description of the basic structural, electronic, vibrational and magnetic properties of these systems.

Standard and hybrid DFT differ in the construction of the many-body exchange and correlation functional. In the Kohn-Sham approach we have adopted the generalized gradient approximation scheme according to Perdew, Burke, and Ernzerhof (PBE),[29] whereas in hybrid DFT (DFTh) a suitable mixing of Hartree-Fock (HF) exchange with the exchange expression of PBE has been used following the HSE03 scheme.[30,31] The resulting expression for the exchange (x) and correlation (c) energy is

$$E_{xc}^{\mathrm{HSE03}} = \frac{1}{4}E_x^{\mathrm{HF,sr},\mu} + \frac{3}{4}E_x^{\mathrm{PBE,sr},\mu} + E_x^{\mathrm{PBE,lr},\mu} + E_c^{\mathrm{PBE}}, \quad (1)$$

in which "sr" and "lr" denote the short- and long-range parts of the respective exchange interactions. The parameter μ controls the range separation: the optimum distance beyond which the short-range interactions become negligible corresponds to values of μ between 0.2 and 0.3 $\mathrm{Å}^{-1}$. We have used $\mu=0.3$ $\mathrm{Å}^{-1}$. As for the mixing parameter $\frac{1}{4}$, although the precise fraction of nonlocal exchange is somewhat system dependent, Perdew *et al.*[32] rationalized that the 25% compromise is superior to purely semilocal functionals.

The Pd(100) substrate was modeled by repeated asymmetric four layers thick slabs which were used as support for the adsorbed Mn_xO_y phases. Most of the calculations have been performed by using two-dimensional (2D) (4×2) and (5×3) unit cells employing the theoretically optimized 2D lattice constant. The corresponding Brillouin-zone integration was done using $6\times6\times1$ and $6\times4\times1$ $\vec{k}$-point grids, respectively, following the Monkhorst-Pack generation scheme. Relaxation of all atomic positions was allowed by minimizing the atomic forces but fixing the position of atoms in the two deepest Pd layers. Albeit the magnetic ordering of the Pd(100)-supported manganese oxide overlayers is unknown, throughout our theoretical investigation we have included spin polarization which allows for a more accurate description of these systems. However, to reduce the already high computational costs, we have limited our inspection to the ferromagnetic (FM) alignment, unless otherwise stated. The vibrational properties have been calculated by diagonalizing the dynamical matrix of the Mn_xO_y subsystems. STM images have been simulated by determining isosurfaces of constant charge, thus following loosely the Tersoff and Hamann method.[33]

Finally, the stability of the most relevant models was underpinned by evaluating the change in the generalized adsorption energy γ upon different concentrations of manganese and oxygen atoms, namely:

$$\gamma = (E_{\mathrm{slab}} - E_{\mathrm{Pd(100)}} - n_{\mathrm{Mn}}\mu_{\mathrm{Mn}} - n_{\mathrm{O}}\mu_{\mathrm{O}}). \quad (2)$$

E_{slab} and $E_{\mathrm{Pd(100)}}$ are the energies of the explored model and of the clean Pd(100) slab, respectively, whereas n_{Mn} and n_{O} are the number of Mn and O atoms for a given model. The reference Mn energy μ_{Mn} is set to the energy of fcc bulk Mn atoms (γ-Mn), while μ_{O} is treated as an extrinsic thermodynamic variable which can be related approximately to the experimental conditions under consideration ($\mu_{\mathrm{O}}=-1.2$ eV, with respect to the free O_2 dimer). We have used a very similar approach for studying the surface phase diagram of MnO(111).[34] A detailed description on the thermodynamic formalism has been presented by Reuter and Scheffler.[35]

The HEX-I and HEX-II phases experimentally observed are found to be incommensurate with (or to have a large coincidence mesh with respect to) the Pd(100) substrate. Therefore, specific to this case, we have performed free-standing calculations (i.e., unsupported Mn_xO_y thin layers). This is a reasonable assumption because the interaction of oxide overlayers with the metallic substrate is found to be relatively weak compared to the interactions within the oxide itself.[36] For this case the stability of a particular structure was evaluated by calculating the formation energy:

$$E_f = (E_{\mathrm{slab}} - n_{\mathrm{Mn}}\mu_{\mathrm{Mn}} - n_{\mathrm{O}}\mu_{\mathrm{O}})/(n_{\mathrm{Mn}} + n_{\mathrm{O}}). \quad (3)$$

III. RESULTS AND DISCUSSION

A. Evidence for two submonolayer regimes

As we have briefly mentioned in Sec. I, the phase diagram of the interfacial Mn oxides on Pd(100) is rather complex and made up of several distinct phases, which have at first sight very little in common as far as their long-range ordering is concerned. Identifying common architectural aspects in these self-organized oxide systems is a major step on the way to rationalize the noticeable complexity and to unravel the driving factors of the architectural flexibility. HREELS offers a valuable diagnostic tool, because it provides the phonon-loss spectrum, which is tightly related to the local arrangement and ion coordination in the smaller building blocks constituting each long-range-ordered phase.[37] In particular, common building blocks shared between different oxide phases are expected to result in similar phonon losses, rendering HREELS sensitive to the occurrence of common structural features.

The HREELS spectra for the four phases considered in the present work are reported in Fig. 2 in the energy range up to 200 meV. All spectra exhibit a clear single peak structure. The phonon loss is centered at around 70 meV for the two hexagonal phases and shifts down to 44–45 meV for the $c(4\times2)$ and CHEV-I phases.[38] Interestingly, the phonon spectra of the CHEV-II, *waves*, and HEX-III phases (not shown), obtained by further lowering the O chemical potential, are also characterized by a single peak at 43–45 meV. These findings provide clear indication of two distinct regimes, an O-rich regime comprising phases with a higher energy phonon loss (70 meV) and an O-poor regime with a single phonon loss around 44 meV. Within each regime, we may surmise that phases with different long-range order possess similar building blocks.[39]

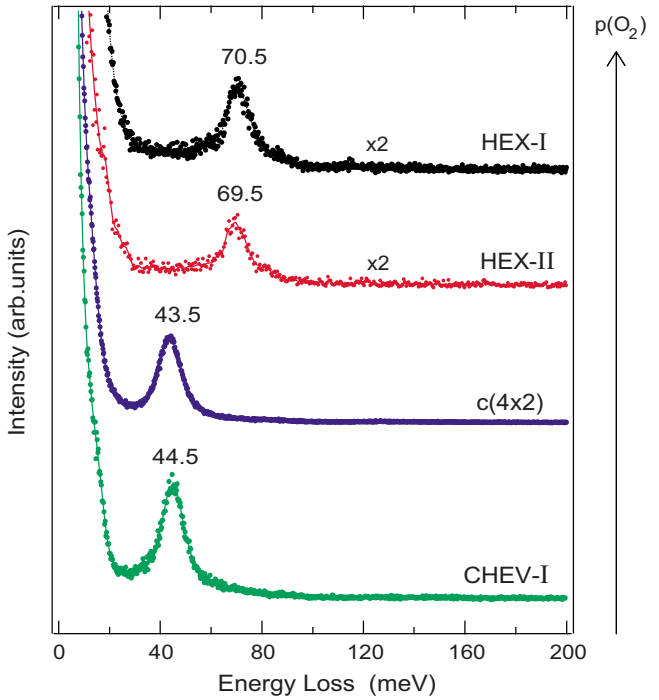

FIG. 2. (Color online) HREELS phonon spectra of the four Mn oxide submonolayer phases discussed in this paper. From the top to the bottom: HEX-I, HEX-II, $c(4\times2)$, and CHEV-I. The statistical uncertainty in the peak position is ±0.5 meV.

Based on the hexagonal symmetry of the more oxidized (HEX-I and HEX-II) phases and on the lattice constant of the HEX-I phase, which is very close to that of bulk MnO(111), one might suggest that these two interfacial phases are related to a MnO(111)-like structure. Conversely, the $c(4\times2)$ phase and by extension the CHEV-I structure might be linked to MnO(100) by analogy with the $c(4\times2)$-Ni_3O_4/Pd(100), precursor of NiO(100) (Refs. 11 and 12) and obtained under similar coverage conditions. To seek support for this assignment we have calculated the dipole active modes for two free-standing MnO(100) and MnO(111) models containing a single manganese layer conveniently oxidized. The calculated phonon losses are reported in Fig. 3 along with a sketch of the corresponding phonon eigenvectors. Indeed, the resulting phonon frequencies, 31 meV and 70–75 meV, unambiguously distinguish two distinct vibrational modes characteristic of the (100) and (111) stacking, respectively. For these specific models PBE and HSE provide essentially the same description: the main MnO(100) dipole active mode at 31 meV originates from the out-of-plane opposite displacements of Mn and O atoms laying on the same plane, whereas the MnO(111) peak at about 75 meV arises from the antiparallel movement of adjacent Mn and O layers. It is therefore natural to associate the calculated (100) and (111) dipole modes with the experimentally observed O-poor (43–45 meV) and O-rich (70 meV) phonon peaks. Consequently, with a certain degree of confidence we conclude that the square (100) and hexagonal (111) MnO thin oxide building units will remain relevant in the interfacial systems grown on Pd(100). Therefore they can be taken as good starting models in the search for realistic structures of the individual phases under consideration, namely, the $c(4\times2)$ and CHEV-I MnO(100)-like structures and the HEX-I and HEX-II MnO(111)-like phases.

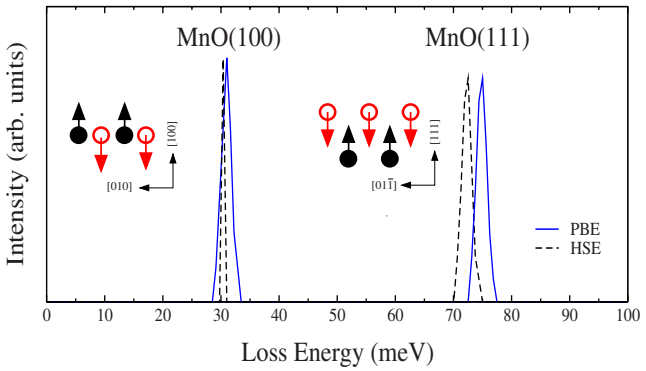

FIG. 3. (Color online) Calculated loss peak spectra for the MnO(100) and MnO(111) unsupported thin oxide layers described in the text. The circle sketches provide a simplified view of the eigenvectors connected to the dipole active modes. Filled and empty circles refer to Mn and O atoms, respectively.

B. MnO(100)-like structures: $c(4\times2)$ and CHEV-I

LEED and STM experiments have shown that an interfacial phase with $c(4\times2)$ symmetry can be stabilized on Pd(100) under suitable conditions.[19] This superstructure appears to be very similar to the recently observed $c(4\times2)$-Ni_3O_4 obtained upon reactive evaporation of nickel on Pd(100),[11,12,40] which has been interpreted as a compressed epitaxial NiO(100) monolayer with a rhombic $c(4\times2)$ array of nickel vacancies. The analogy is not surprising if one considers the nature of the two oxide systems. Indeed, strong similarities exist between NiO and MnO in terms of structural properties (same rhombohedrally distorted fcc structure), magnetic ordering (same antiferromagnetic type-II spin ordering), and electronic character (partially filled localized *d* states). Furthermore, bulklike MnO(100) (Ref. 17) and NiO(100) (Ref. 20) films can be both grown on a Pd(100) substrate.

Prompted by the strong similarities between the two $c(4\times2)$ phases and guided by the structural analysis on the $c(4\times2)$-Ni_3O_4/Pd(100) phase[11,12,40] we have compared the relative stabilities of a number of different models resembling the Ni_3O_4-$c(4\times2)$ geometry. The models are constructed by placing a compressed MnO(100) monolayer on top of a four layer Pd(100) substrate and creating Mn vacancies with a rhombic (RH) $c(4\times2)$ symmetry. The lateral compression compensates for the positive mismatch between MnO(100) ($a_{MnO}=3.09$ Å, PBE) and Pd(100) ($a_{Pd}=2.79$ Å, PBE). Three options have been considered concerning the lateral registry: (RH1) oxygen atoms placed on top of Pd with the manganese species sitting in hollow sites; (RH2) the configuration opposite to RH1 with manganese arranged on top of Pd; and (RH3), with both Mn and O in bridge sites. As for the magnetic ordering, we have explored the FM arrangement and two different antiferromagnetic configurations of the Mn spins. A detailed description of the calculations will be given elsewhere.[41] For the present purposes it is essential to point out that the FM RH1 structure, schematically de-

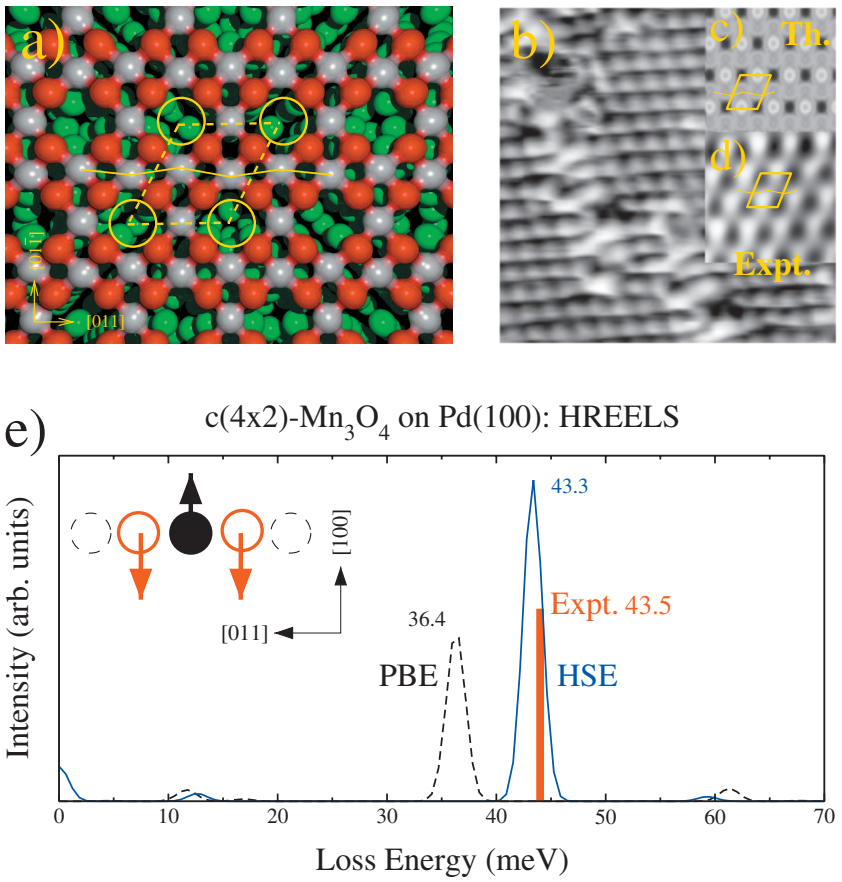

FIG. 4. (Color) (a) Top view of the geometrical model for the Pd(100)-supported $c(4\times2)$-Mn_3O_4 phase: red spheres: O atoms; light gray spheres: Mn atoms; green small spheres: Pd atoms underneath. Dashed lines delimit the 2D unit cell, the full line indicates the manganese lateral displacements, and circles highlight the position of the vacancies. (b) Experimental STM image of the $c(4\times2)$-Mn_3O_4 phase; sample bias $U=+0.5$ V; tunneling current $I=0.2$ nA. [(c) and (d)] High-resolution (c) simulated and (d) experimental STM images taken at sample bias $U=+1.0$ V; tunneling current $I=0.25$ nA. The theoretical image has been calculated considering tunneling into empty states between 0 and +0.5 eV. Full lines indicate the 2D unit cell and the zigzag Mn chain. (e) Comparison between the measured HREELS phonon value (vertical bar) and PBE (dashed line) and HSE (full line) predicted dipole active modes for the $c(4\times2)$-Mn_3O_4 phase. The inset schematically depicts the atomic displacements giving rise to the calculated phonon peaks. Mn and O atoms are sketched as filled and empty circles, respectively. The dashed line circles indicate the vacancies.

picted in Fig. 4(a), results as the most favorable one, at least 200 meV more stable than all other considered models. The fully optimized structure consists of a corrugated MnO(100) adlayer whose average distance from the substrate (2.42 Å) is 22% larger than the Pd(100) interlayer spacing. The corrugation of ≈0.23 Å arises from the outward displacement of the oxygen atoms. In the layer plane we find a negligible displacement of the oxygen atoms from their on-top positions, but a small shift (0.16 Å) along the [01$\bar{1}$] direction experienced by the Mn atoms. This displacement toward the vacancy clearly is the result of the free space and charge left by the missing manganese and acts to release the compressive strain in the Mn-O overlayer. The rearrangements of the Mn species, also highlighted by the full line in Fig. 4(a), results in a zigzag Mn-Mn chain along [011] which was also observed in the $c(4\times2)$-Ni_3O_4 system.

In Figs. 4(b)–4(d) we compare experimental and calculated STM images of $c(4\times2)$-Mn_3O_4. The close resemblance between the STM simulation [inset (c)] and the high-resolution STM image [Fig. 4(d)] allows us to discuss further atomic details of the RH1 model. Atomic resolution reveals that the RH1 unit cell consists of different subunits made up of bright spots with different contrast and black holes spanning the 2D unit cell. The rhombic array of dark depressions, separated by a distance of 5.58 Å, reflects the network of Mn vacancies encircled in Fig. 4(a), whereas the light protrusions result from the remaining Mn species. The strong structural rearrangement induced by the lattice mismatch and by the creation of a Mn vacancy is reflected in the STM spots: the single bright features can be assigned to the Mn species sandwiched between two vacancies, whereas the light rows developing along the [011] direction are interpreted as zigzagging Mn-Mn chains embedded in a regular oxygen array (laying ≈0.23 Å higher).

Further support for the proposed $c(4\times2)$-Mn_3O_4 surface structure is provided by the comparison of the calculated phonon spectrum with the HREELS measurements [Fig. 4(e)]. Remarkably, the single peak structure centered at ≈43.5 meV revealed by HREELS is very well reproduced by our calculations. Although standard DFT underestimates the phonon energy by ≈7 meV, the inclusion of a portion of

Hartree-Fock exchange within the HSE method improves significantly the agreement with the experimentally measured value. The diagonalization of the dynamical matrix enables to assign this specific phonon mode to the antiphase out-of-plane vibrations of surface O and Mn atoms, as schematically depicted in the inset of Fig. 4(e). This vibrational mode is very similar to that found for the MnO(100) unsupported thin film (Fig. 3) thus reflecting the MnO(100)-like nature of the RH $c(4\times2)$-Mn_3O_4 phase.

Despite the striking similarity between the two $c(4\times2)$ monolayer structures formed by Ni and Mn oxides on Pd(100), precursor phases of NiO(100) and MnO(100), an important difference can be highlighted when considering the lattice mismatch between the two bulk oxides and the Pd(100) substrate. The experimental mismatch is in fact $\approx$7% and 14% for NiO(100) and MnO(100), respectively, indicating that the $c(4\times2)$ formed by Mn oxide is subjected to a much higher compressive stress. This is reflected in the experimental STM images [Fig. 4(b)], which show ordered regions bearing the $c(4\times2)$-Mn_3O_4 periodicity separated by regions of defects. The incorporation of extensive defect areas into the film presumably arises from the release of the high compressive strain. The latter might also explain the tendency of the $c(4\times2)$-Mn_3O_4 structure to nucleate preferentially near step edges. Moreover, we have observed that a remarkably well-ordered $c(4\times2)$ overlayer forms on Pd(1 1 19),[42] where (100) terraces exposing ten atomic rows are separated by a regular array of monoatomic steps. Clearly, the steps provide a suitable means of lateral relaxation and thus enable to achieve stress relief in a natural way. It is also worth noting that the high surface stress in the $c(4\times2)$ phase may be responsible for its tendency to transform into a *stripe* phase (Fig. 1), which can be interpreted as a distorted $c(4\times2)$ and is obtained at comparable values of the oxygen chemical potential.[19]

We now turn our attention to the CHEV-I structure which is adjacent to the $c(4\times2)$ in the phase diagram and is obtained by lowering the O_2 pressure during the preparation. This structure can be prepared as a single phase by postoxidation method, as assessed by LEED and STM. However, the STM images also show that it can coexist locally with both the $c(4\times2)$ and CHEV-II phases, as illustrated in panel (a) of Fig. 5. Here, it appears clearly that the $c(4\times2)$ and CHEV-I structures transform smoothly into each other, a strong indication that they possess not only similar energetics but also common structural features. Indeed, as it can be seen by inspection of the real-space models in Figs. 5(b) and 5(c), the CHEV-I periodicity can be naturally obtained from the $c(4\times2)$ by extending one lattice vector to a neighboring antiphase position, thus yielding a structure with the matrix notation reported in Fig. 5(c). As discussed above, the periodicity of the $c(4\times2)$ model is given by the Mn vacancies. Within this picture, the CHEV-I structure may be described in terms of the propagation of a Mn vacancy as indicated by the arrow in Fig. 5(c). Accordingly, the stoichiometry becomes Mn_6O_7, i.e., closer to that of MnO. Compared to the $c(4\times2)$ phase, the CHEV-I structure exhibits a much higher degree of long-range order, with large defect-free areas extending over typical distances of 200 Å and interrupted by ordered domain boundaries, which convey the characteristic chevronlike appearance[19] [see also Fig. 5(a)].

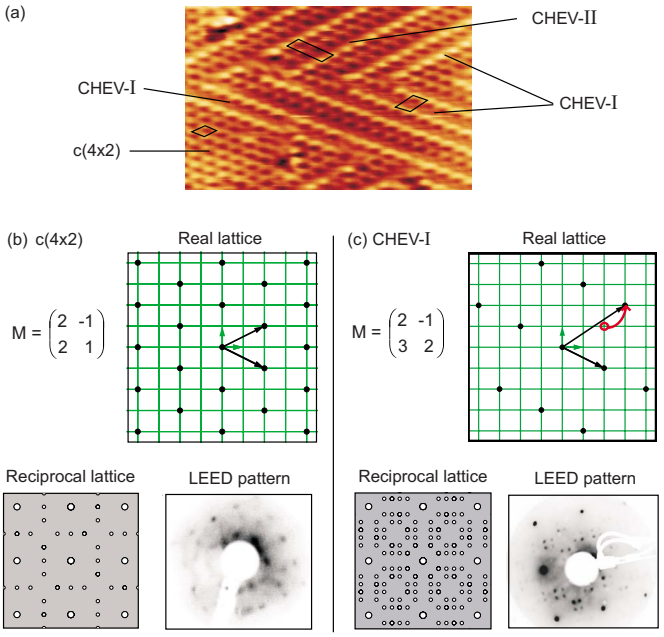

FIG. 5. (Color online) (a) STM image showing the characteristic appearance of the *chevrons* structures and the local coexistence of the $c(4\times2)$, CHEV-I, and CHEV-II phases (140 Å$\times$100 Å; $U=+1.0$ V; $I=0.2$ nA). [(b) and (c)] Real lattice, reciprocal lattice, and experimental LEED pattern ($E=110$ eV) for the [panel (b)] $c(4\times2)$ and [panel (c)] CHEV-I structures. The arrow in the top right panel shows how the periodicity of the CHEV-I structure can be obtained from the $c(4\times2)$ periodicity by extending one of the two lattice vectors to a neighboring antiphase position.

Following the above arguments and encouraged by the detailed description of the $c(4\times2)$ phase in terms of the RH1 Mn_3O_4 model, we tested the vacancy propagation model adopting the above-mentioned Mn_6O_7 structure. This model is constructed by removing 14% of Mn ions from the compressed MnO(100) layer as sketched in Fig. 6(a). The geometrical optimization yields again an oxygen-terminated surface with a corrugation of 0.33 Å. In analogy with the $c(4\times2)$-Mn_3O_4 structure we observe a small displacement (0.13 Å) of manganese atoms toward the vacancy [see arrows in Fig. 6(a)]. Figure 6(b) shows a comparison between the experimental and simulated STM images. Although the experimental resolution does not allow for an unambiguous atomic comparison between theory and experiment, the overall agreement is satisfactory. The dark circular depressions in the image represent the position of the Mn vacancies and determine the 2D unit cell of this phase, as outlined by the full lines. The bright protrusions are clearly due to manganese atoms, suggesting that electronic effects contribute predominantly to the STM topography. Two distinct bright features are observed in the experimental picture, one large spot in the center of the unit cell and weaker flecks on the edges. The simulated STM image together with the optimized geometrical data allow for an atomically resolved identification of these two kinds of features. The manganese sublayer is itself slightly corrugated, due to a small upward shift (0.05 Å) of the Mn atoms laying closer to the vacancy and

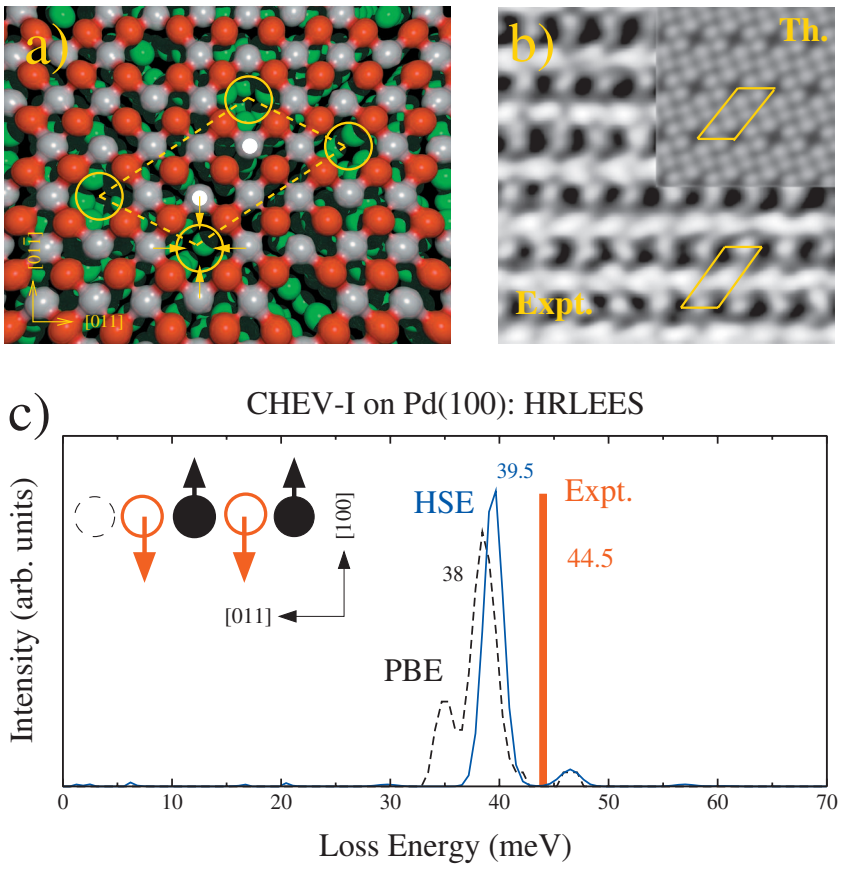

FIG. 6. (Color) (a) Top view of the geometrical model for the Pd(100) supported CHEV-I Mn_6O_7 phase: red (dark gray) spheres: O atoms; light gray spheres: Mn atoms; green (gray) small spheres: Pd atoms underneath. Dashed lines delimit the 2D unit cell and circles highlight the position of the vacancies. (b) Experimental and simulated STM images of the CHEV-I phase; sample bias $U=+1.0$ V; tunneling current $I=0.13$ nA. The simulated STM image has been calculated considering tunneling into empty states between 0 and +1.0 eV. Unit cells are indicated by full lines. (c) Comparison between the measured HREELS phonon value (vertical bar) and PBE (dashed line) and HSE (full line) predicted dipole active modes for the CHEV-I phase. The inset schematically depicts the atomic displacements giving rise to the calculated phonon peaks. Mn and O atoms are sketched as filled and empty circles, respectively. The dashed line circle denotes a vacancy.

aligned in the $[01\bar{1}]$ direction. These atoms, outlined by filled dots in Fig. 6(a), are responsible for the two large bright spots in the simulated STM image and should be connected to the lines of bright protrusions seen in the experimental STM image. The remaining spots (four per unit cell) arise from the lower manganese atoms. In the experimental STM image their intensity partially mixes up with the topmost Mn spots thus contributing to the large bright feature centered in the cell and partially providing the weaker spots along the edges.

Finally, our DFTh calculations establish [Fig. 6(c)] that the proposed Mn_6O_7 model is characterized by a single dipole active mode located at around 40 meV, only 4 meV lower than the measured loss energy. This peak reflects the vibrational character of the parent MnO(100) not only in terms of phonon-loss energy, very similar to the $c(4\times2)$-Mn_3O_4 value, but also in terms of the atomic displacements producing this vibration. As sketched in the inset of Fig. 6(c), the peak originates from the antiphase out-of-plane movements of manganese and oxygen atoms.

C. MnO(111)-like structures: HEX-I and HEX-II

In the oxygen-rich regime, the experiments show that the most stable phase in a broad range of pressures above 5×10^{-7} mbar is the HEX-I phase, which may be linked to MnO(111). The structure of bulk MnO(111) is made out of alternating O and Mn layers, having in-plane hexagonal arrangement with lattice constant $a_{MnO}=3.14$ Å [see Fig. 7(a)]. A perfect MnO(111) film would give rise to a hexagonal reciprocal space pattern with a lattice constant $4\pi/3a_{MnO}=2.30$ Å^{-1}, which is very close to the reciprocal Pd(100) lattice parameter ($2\pi/a_{Pd}=2.28$ Å^{-1}). The resulting LEED pattern averaged over two hexagonal domains rotated by 90°, which account for the different symmetry of substrate and overlayer, is a circular array of 12 extra spots superimposed on the ten spots of the substrate, as illustrated in Fig. 7(b). Such a LEED pattern has been indeed observed in the experiments, as demonstrated in Fig. 7(c). Here, additional faint spots with $c(6\times2)$ symmetry are also observed, which arise from the coincidence mesh between substrate and overlayer.[43]

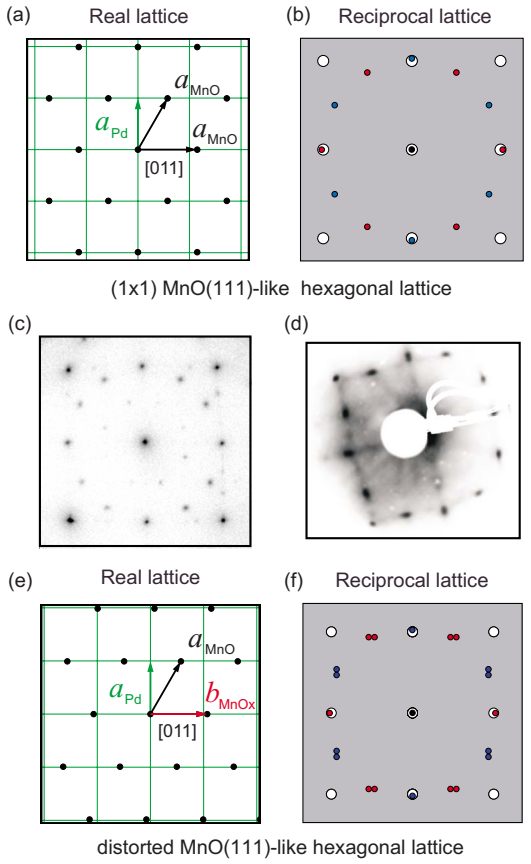

FIG. 7. (Color online) (a) Real and (b) reciprocal lattice for a (1×1) MnO(111)-like hexagonal structure on a Pd(100) surface. The lattice parameter of the overlayer is assumed to be the measured bulk value $a_{MnO}=3.14$ Å, whereas $a_{Pd}=2.75$ Å. In (a) only one of the two symmetry domains is reported for clarity. (c) SPA-LEED two-dimensional pattern measured at $E=90$ eV, for the undistorted HEX-I phase. (d) LEED pattern of the distorted HEX-I phase, recorded at $E=96$ eV. (e) Real and (f) reciprocal lattice associated with the distorted hexagonal MnO(111)-like phase. Only one symmetry domain is shown in (e) for clarity, for which the lattice parameter in the [011] direction of the distortion is $b_{MnO_x}=2.94$ Å. In total, four symmetry domains contribute to the reciprocal lattice in (f): two are obtained from panel (e) with a_{MnO} at either +60° or −60° from b_{MnO_x}, and the other two are obtained by rotating a_{MnO} by 90° relative to the substrate mesh.

A similar LEED pattern has been also obtained at comparable coverage for oxidized Mn on Rh(100) and attributed to MnO(111).[44] For Mn oxide nanolayers on Pd(100), however, it has not been observed always reproducibly in the different experimental systems. It appears that this structure is favored at a slightly lower coverage (0.5–0.6 ML) or after repeated oxidation cycles. Thus, the experimental evidence suggests that this "perfect" (1×1) structure may have limited stability on Pd(100) or may be kinetically stabilized. In contrast, the LEED pattern shown in Fig. 7(d) was reproducibly obtained after oxidation at high pressure of 0.75 ML. Here, the characteristic elongation of the overlayer spots indicates a distortion of the perfect (1×1) structure. It consists of either a contraction of one lattice vector or a reduction in the 60° angle of the 2D hexagonal cell. The first type of distortion explains successfully the moiré pattern observed in the STM images [see Fig. 8(c)]: by reducing the lattice vector along [011] to $b_{MnO_x}=2.94$ Å [Fig. 7(e)] the experimentally observed moiré periodicity of ≈22 Å along this direction is correctly reproduced[19] and the LEED spots appear elongated or split [Fig. 7(f)]. By inspection of Figs. 7(a) and 7(e), one may infer that the closer matching between the overlayer and substrate meshes is the driving force for the distortion: the initial mismatch of 14% along the [011] direction is in fact reduced to $(b_{MnO_x}-a_{Pd})/a_{Pd}=7\%$. This better epitaxial relationship is presumably at the origin of the increased stability of the distorted HEX-I phase.

As already pointed out in Sec. II B the computational modeling of the HEX-I and HEX-II phases has to be done with the unsupported setup, namely, considering only free-standing thin layers. The most natural way to construct such hexagonal thin Mn-O layers is by cleaving MnO perpendicular to the [111] direction. In the rocksalt (111) stacking the smallest blocks containing 1 ML of Mn atoms are either a Mn-O bilayer or an O-Mn-O trilayer. We have first studied the relative stability of these two configurations by minimizing the formation energy with respect to the 2D hexagonal lattice constant. The computed energies E_f, plotted in Fig. 9, clearly show that the trilayer structure, with a formal stoichiometry of MnO_2, is by far more favorable in a wide portion of the phase diagram than the bilayer MnO structure. Only in the oxygen-poor regime the bilayer gains stability with respect to the trilayer. However, the latter conditions are unrealistic compared to the experimental situation $(\approx10^{-6}$ mbar).

A rigid sphere sketch of the MnO_2 trilayer is given in Fig. 8(a). As a direct consequence of the free-standing nature, the minimized planar lattice constant, $a=2.89$ Å, is considerably smaller than the corresponding calculated bulk lattice constant of 3.09 Å. For the same reason, the optimized interlayer distance, 0.95 Å, is found to be 25% shorter than the bulk value. In a second step, in order to simulate the experimentally observed distorted hexagonal structure we have computed the energy required to distort the perfect hexagonal trilayer by shrinking the lattice constant b by 7%. We found that the distorted trilayer is only 70 meV less stable than the perfect hexagonal trilayer, as shown in the phase diagram of Fig. 9. Therefore, although we find that the perfect hexagonal structure is the most favorable, only a low energy cost is required to convert it into a distorted hexagonal structure. Considering that our model neglects the effect of the Pd(100) substrate and that the distortion allows for a better lattice matching with the substrate, we conclude that the distorted trilayer model of the HEX-I is also supported by our calculations. We have tested the soundness of the proposed MnO_2 trilayer model by comparing the experimental STM and HREELS data with the theory. The results are presented in Figs. 8(c)–8(f). As evident from Fig. 8(c) the HEX-I phase displays the moirè-like superstructure already discussed.[19] The atomically resolved STM shown in panel (d) provides information on the local hexagonal symmetry of the array of bright protrusions, while panel (e) gives the result of the simulation. We find a fair agreement between the two images, and the theoretical data allow us to assign the bright spots to the topmost oxygen atoms. Convincing addi-

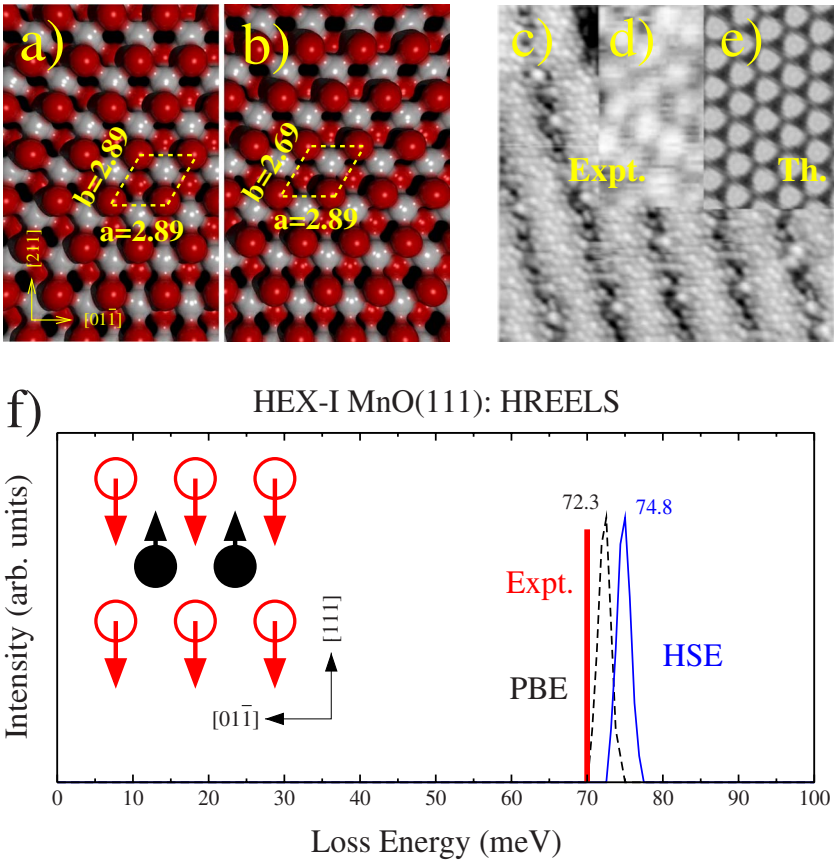

FIG. 8. (Color online) [(a) and (b)] Top view of geometrical models for unsupported (a) HEX-I MnO(111) and distorted (b) HEX-I MnO(111) phases: red (dark gray) spheres: O atoms; light gray spheres: Mn atoms. Dashed lines delimit the 2D unit cell. [(c)–(e)] [(c) and (d)] Experimental and (e) simulated STM images of HEX-I; experimental images: sample bias (c) $U=+0.5$ V, (d) +0.6 V; tunneling current (c) $I=0.13$ nA, (d) 0.15 nA. The simulated STM image has been calculated considering tunneling into empty states between 0 and +0.5 eV. (f) Comparison between the measured HREELS phonon value (vertical bar) and PBE (dashed line) and HSE (full line) predicted dipole active modes for the HEX-I phase. The inset schematically depicts the atomic displacements giving rise to the calculated phonon peaks. Mn and O atoms are sketched as filled and empty circles, respectively.

tional support for our model comes from the comparison between the experimental and calculated phonon spectra of Fig. 8(f). DFT and DFTh locate the distinct dipole active mode between 72 and 75 meV, which is only a few meV higher than the measured value of 70.5 meV. The displacements corresponding to this mode, sketched in the inset, clearly show that this particular vibration is linked to the alternately stacked hexagonal layers of manganese and oxygen atoms along the direction perpendicular to the surface and is not compatible with the MnO(100)-like monolayer. It is also worth noting that the trilayer model is consistent with the O 1*s* core-level photoemission data presented in Ref. 19, which hint at the presence of two O 1*s* components separated by roughly 0.4 eV in binding energy. In fact, the stronger photoemission component at 529.1 eV can be assigned to the surface O layer, whereas the weaker line at higher binding energy can be related to the O layer at the interface with the Pd(100) substrate, in close analogy with previous assignments for trilayer oxide systems.[45,46]

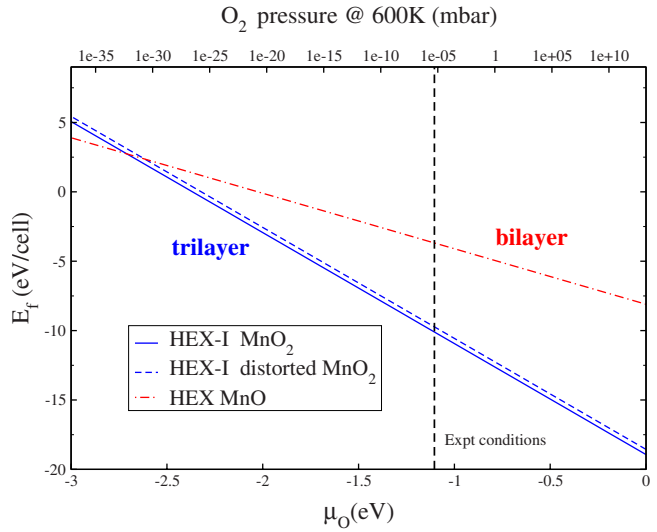

FIG. 9. (Color online) Thermodynamic DFT phase stability diagram of explored HEX-I models in equilibrium with an O particle reservoir controlling the chemical potential μ_O. The top scale is converted into oxygen pressure.

The O-Mn-O MnO(111) trilayer model is the natural starting point for the structural understanding of the HEX-II phase which is obtained from the HEX-I phase upon reduction in the oxygen partial pressure. We rely on our previous work on the reconstruction of the bulk-terminated MnO(111) surface,[34] which allows us to restrict significantly the structural search. The STM and LEED analyses provide clear evidence for a well-ordered 2D hexagonal unit cell with lattice constant $a \approx 6.0$ Å (Ref. 19), corresponding to a compressed (2×2) reconstruction of the MnO(111) termination. Our DFT calculations revealed that all reconstructions with (2×2) periodicity are more stable than others with (2×1) or $(\sqrt{3}\times\sqrt{3})$ symmetry. Among the explored (2×2) structures we found that an oxygen-terminated octopolar reconstruction and a so-called α phase display the lowest surface energies in a wide range of oxygen partial pressure. Hence, we have focused our search on related (2×2) structures, limiting the exploration to thin layers containing $\lesssim 1$ ML Mn. The octo-

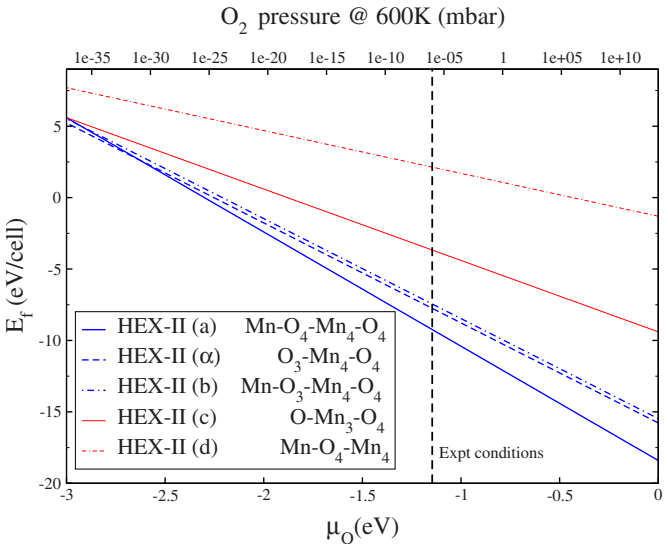

FIG. 10. (Color online) Thermodynamic DFT phase stability diagram of explored HEX-II models in equilibrium with an O particle reservoir controlling the chemical potential μ_O. The top scale is converted into oxygen pressure.

polar reconstruction contains local pyramidal structures obtained by removing one quarter of atoms from the subsurface and three quarters from the surface layer. It consists of triangular based pyramids with either O-Mn_3-O_4 or Mn-O_3-Mn_4 stacking, respectively. Instead, the α structure is obtained by removing the topmost atom from the octopolar reconstruction, resulting in a Mn_3-O_4 (Mn-terminated) or O_3-Mn_4 (O-terminated) stoichiometry. In addition to the stoichiometrically perfect octopolar and α reconstructions we have also considered slightly modified models, obtained by suitable addition or removal of one surface or subsurface atom. In Fig. 10 we summarize the phase diagram of the most stable models explored. We first point out that all quasibilayer models (with adatoms) such as HEX-II (c) and HEX-II (d) are less favorable. Conversely, the models that maintain a trilayer nature compatible with the octopolar and α reconstructions are clearly preferred, such as HEX-II (a), HEX-II α, and HEX-II (b).

Let us now focus on the two most stable models, HEX-II (a) and HEX-II α, whose schematic view is given in Figs. 11(a) and 11(b). HEX-II (a) is obtained by adding one manganese atom on top of the HEX-I trilayer, whereas HEX-II α is the stoichiometrically perfect oxygen-terminated α reconstruction, built by removing one surface oxygen atom per (2×2) unit cell from the HEX-I structure. At first glance HEX-II (a) appears to be the most favorable model, but a deeper inspection leads to a different conclusion. We first note that the Mn coverage of HEX-II (a) is 1.25 ML, i.e., larger than the experimental one, and that the optimized planar lattice constant for the HEX-II (a) model, 5.78 Å, is smaller than the measured value of 6.0 Å. Conversely, the O-terminated α model has the right Mn coverage of 1 ML, and its relaxed lattice constant is 5.95 Å, i.e., almost identical to the experimental value. Moreover, compelling evidence for the O-terminated α phase comes from the comparison between the simulated STM and HREELS data and the corresponding experimental results given in Figs. 11(c) and 11(d), respectively. The STM image reveals a hexagonal pattern of large bright triangular intensity maxima well reproduced by the simulated STM image. The latter display triangular protrusions, which are ascribed to the oxygen trimers outlined in the sketch of panel (b). Instead, the simulated HEX-II (a) STM image (not shown) is characterized by circular bright protrusions. As for the HREELS spectrum, in analogy with its precursor, the HEX-I phase, the HEX-II α displays a single peak centered at 69.5 meV, characteristic of the MnO(111)-like structures. The simulation reproduces well the position of the vibrational peak and ascribes it to the concerted movement of the surface oxygen trimers against the manganese atoms underneath. In contrast, the calculated dipole active mode for the HEX-II (a) model is significantly higher in energy, 83 meV, and comes from a different kind of displacement, namely, the vertical vibration of the octopolar Mn apex against the triangular oxygen basis. Taken together, it appears that the α structure is the best of the explored models in reproducing the experimental scenario in terms of structural properties, vibrational spectra, and STM images. Although the HEX-II (a) phase is energetically competitive and even somewhat preferred, other calculated properties such as the dipole active mode and STM image do not match as well with the experimental data.

IV. SUMMARY AND CONCLUSIONS

The Mn_xO_y/Pd(100) system possesses a complex and intriguing phase diagram. In previous work[17,18] we have described the high coverage regime (15–20 ML), where well-ordered bulklike MnO(100) films can be grown in a wide range of temperature and pressure, which in turn can be converted either into MnO(111) or Mn_3O_4(001) structures by tuning the appropriate conditions of temperature and pressure. At (sub)monolayer coverages an even richer phase diagram is found, which comprises nine different structures (Fig. 1). Here, by means of combined experimental and theoretical tools we have carried out a detailed investigation on four prototypical phases [$c(4\times2)$, CHEV-I, HEX-I, and HEX-II], which belong to two distinct oxygen pressure regimes and are characterized by well-defined structural and vibrational properties.

At oxygen-poor conditions a two-dimensional $c(4\times2)$-Mn_3O_4 structure is stable, which is described as a MnO(100) monolayer with a rhombic array of manganese vacancies, in close analogy to the $c(4\times2)$-Ni_3O_4/Pd(100) structure.[11,12,40] Upon reduction, vacancy propagation leads to the Mn_6O_7 CHEV-I phase, also representing a monolayer structure. The close structural relation between CHEV-I and $c(4\times2)$ is reflected in the common vibrational fingerprint, with a single HREELS loss peak at $\approx$44 meV due to the antiphase out-of-plane movements of almost coplanar Mn and O ions.

In the oxygen-rich regime the scenario changes substantially. The observed HEX-I and HEX-II phases possess a MnO(111)-derived O-Mn-O trilayer structure and display the

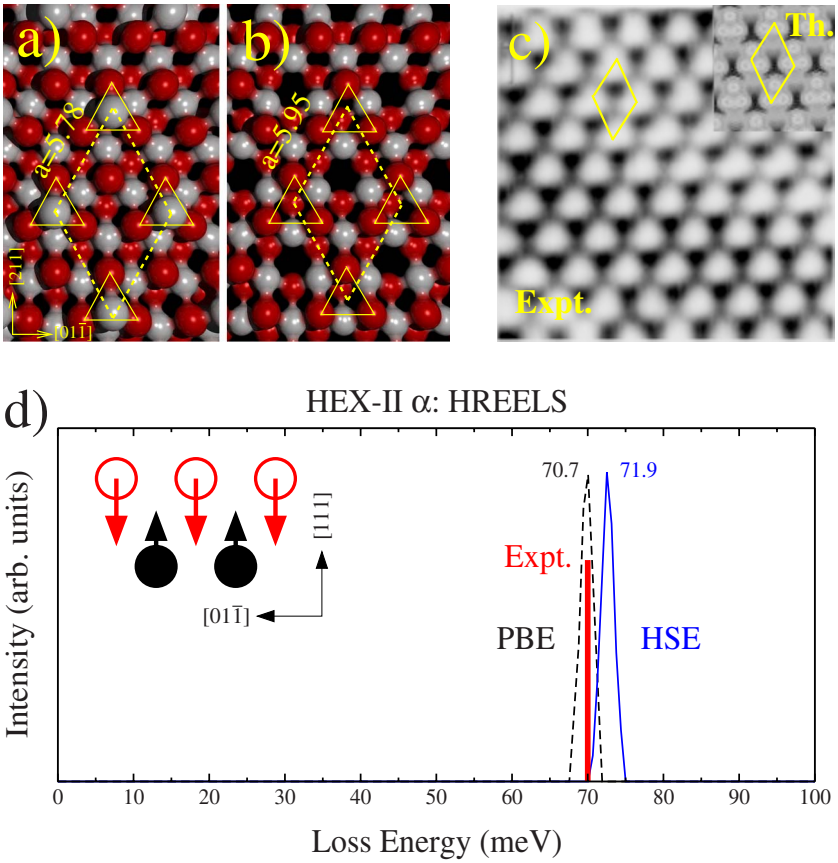

FIG. 11. (Color online) [(a) and (b)] Top view of the two most stable models for unsupported HEX-II, namely, (a) octopolarlike Mn_5O_8 and (b) Mn_4O_7-α phases: red (dark gray) spheres: O atoms; light gray spheres: Mn atoms. Dashed lines delimit the 2D unit cell, whereas triangles highlight the octopolar Mn-O_3 pyramids and the O_3 trimers of the α termination. (c) Experimental and simulated STM images of the hexagonal α HEX-II phase; sample bias $U=+0.75$ V; tunneling current $I=0.1$ nA. The simulated STM images have been calculated considering tunneling into empty states between 0 and +0.75 eV. Unit cells are indicated by full lines. (d) Comparison between the measured HREELS phonon value (vertical bar) and PBE (dashed line) and HSE (full line) predicted dipole active modes for the α HEX-II phase. The inset schematically depicts the atomic displacements giving rise to the calculated phonon peaks. Mn and O atoms are sketched as filled and empty circles, respectively.

same dipole active mode at ≈70 meV. The transition between HEX-I and HEX-II is driven by the formation of oxygen vacancies inducing a so-called α reconstruction and changing the stoichiometry from MnO_2 to Mn_4O_7. Incidentally, the occurrence of similar trilayer models has been also invoked to describe other transition-metal (Rh and Ir) surface oxides.[45–47] The correct assignment and atomic-level description of all structures is validated by the excellent agreement between experiment and theory in terms of structural and vibrational properties.

ACKNOWLEDGMENTS

This work was supported by the Austrian Science Funds FWF within the Joint Research Program S90 and the Science College W4, and by the 6th Framework Programme of the European Community (GSOMEN).

*cesare.franchini@univie.ac.at
†francesco.allegretti@uni-graz.at

[1] M. Ritter, W. Ranke, and W. Weiss, Phys. Rev. B **57**, 7240 (1998).
[2] L. Giordano, G. Pacchioni, J. Goniakowski, N. Nilius, E. D. L. Rienks, and H.-J. Freund, Phys. Rev. B **76**, 075416 (2007).
[3] S. Shaikhutdinov, M. Ritter, and W. Weiss, Phys. Rev. B **62**, 7535 (2000).
[4] G. Ketteler and W. Ranke, J. Phys. Chem. B **107**, 4320 (2003).
[5] S. Surnev, L. Vitali, M. G. Ramsey, F. P. Netzer, G. Kresse, and J. Hafner, Phys. Rev. B **61**, 13945 (2000).
[6] S. Surnev, G. Kresse, M. G. Ramsey, and F. P. Netzer, Phys. Rev. Lett. **87**, 086102 (2001).
[7] S. Surnev, G. Kresse, M. Sock, M. G. Ramsey, and F. P. Netzer,

Surf. Sci. **495**, 91 (2001).
[8] J. Schoiswohl, S. Surnev, F. P. Netzer, and G. Kresse, J. Phys.: Condens. Matter **18**, R1 (2006).
[9] J. Schoiswohl, G. Kresse, S. Surnev, M. Sock, M. G. Ramsey, and F. P. Netzer, Phys. Rev. Lett. **92**, 206103 (2004).
[10] J. Schoiswohl, M. Sock, S. Eck, S. Surnev, M. G. Ramsey, F. P. Netzer, and G. Kresse, Phys. Rev. B **69**, 155403 (2004).
[11] S. Agnoli, M. Sambi, G. Granozzi, A. Atrei, M. Caffio, and G. Rovida, Surf. Sci. **576**, 1 (2005).
[12] S. Agnoli, M. Sambi, G. Granozzi, J. Schoiswohl, S. Surnev, F. P. Netzer, M. Ferrero, A. M. Ferrari, and C. Pisani, J. Phys. Chem. B **109**, 17197 (2005).
[13] M. Caffio, B. Cortigiani, G. Rovida, A. Atrei, and C. Giovanardi, J. Phys. Chem. B **108**, 9919 (2004).
[14] M. Caffio, A. Atrei, B. Cortigiani, and G. Rovida, J. Phys.: Condens. Matter **18**, 2379 (2006).
[15] W. Meyer, D. Hock, K. Biedermann, M. Gubo, S. Müller, L. Hammer, and K. Heinz, Phys. Rev. Lett. **101**, 016103 (2008).
[16] C. Hagendorf, S. Sachert, B. Bochmann, K. Kostov, and W. Widdra, Phys. Rev. B **77**, 075406 (2008).
[17] F. Allegretti, C. Franchini, V. Bayer, M. Leitner, G. Parteder, B. Xu, A. Fleming, M. G. Ramsey, R. Podloucky, S. Surnev, and F. P. Netzer, Phys. Rev. B **75**, 224120 (2007).
[18] V. Bayer, R. Podloucky, C. Franchini, F. Allegretti, B. Xu, G. Parteder, M. G. Ramsey, S. Surnev, and F. P. Netzer, Phys. Rev. B **76**, 165428 (2007).
[19] F. Li, F. Allegretti, G. Parteder, C. Franchini, R. Podloucky, S. Surnev, and F. P. Netzer, arXiv:0811.4555, J. Phys.: Condens. Matter (to be published 2009).
[20] J. Schoiswohl, W. Zheng, S. Surnev, M. G. Ramsey, G. Granozzi, S. Agnoli, and F. P. Netzer, Surf. Sci. **600**, 1099 (2006).
[21] I. Kardinal, F. P. Netzer, and M. G. Ramsey, Surf. Sci. **376**, 229 (1997).
[22] Reported pressures were not corrected for the ion gauge sensitivity.
[23] P. E. Blöchl, Phys. Rev. B **50**, 17953 (1994).
[24] G. Kresse and D. Joubert, Phys. Rev. B **59**, 1758 (1999).
[25] G. Kresse and J. Furthmüller, Comput. Mater. Sci. **6**, 15 (1996).
[26] C. Franchini, V. Bayer, R. Podloucky, J. Paier, and G. Kresse, Phys. Rev. B **72**, 045132 (2005).
[27] C. Franchini, R. Podloucky, J. Paier, M. Marsman, and G. Kresse, Phys. Rev. B **75**, 195128 (2007).
[28] V. Bayer, C. Franchini, and R. Podloucky, Phys. Rev. B **75**, 035404 (2007).
[29] J. P. Perdew, K. Burke, and M. Ernzerhof, Phys. Rev. Lett. **77**, 3865 (1996).
[30] J. Heyd, E. Scuseria, and M. Ernzerhof, J. Chem. Phys. **118**, 8207 (2003).
[31] J. Paier, R. Hirschl, M. Marsman, and G. Kresse, J. Chem. Phys. **122**, 234102 (2005).
[32] J. P. Perdew, M. Ernzerhof, and K. Burke, J. Chem. Phys. **105**, 9982 (1996).
[33] J. Tersoff and D. R. Hamann, Phys. Rev. B **31**, 805 (1985).
[34] C. Franchini, V. Bayer, R. Podloucky, G. Parteder, S. Surnev, and F. P. Netzer, Phys. Rev. B **73**, 155402 (2006).
[35] K. Reuter and M. Scheffler, Phys. Rev. B **65**, 035406 (2001).
[36] G. Kresse, S. Surnev, M. G. Ramsey, and F. P. Netzer, Surf. Sci. **492**, 329 (2001).
[37] S. Surnev, M. Sock, G. Kresse, J. N. Andersen, M. G. Ramsey, and F. P. Netzer, J. Phys. Chem. B **107**, 4777 (2003).
[38] For every Mn oxide phase, measurements performed on samples freshly prepared in different days agree within 1 meV.
[39] We found further evidence for the existence of two different regimes in x-ray photoemission and absorption experiments with synchrotron radiation.
[40] A. M. Ferrari, M. Ferrero, and C. Pisani, J. Phys. Chem. B **110**, 7918 (2006).
[41] C. Franchini, F. Allegretti, F. Li, S. Surnev, F. P. Netzer, and R. Podloucky (unpublished).
[42] F. Li, F. Allegretti, S. Surnev, and F. P. Netzer (unpublished).
[43] A $c(6\times2)$ coincidence net is only obtained when a_{MnO} is expanded by $\approx3\%$. A perfect MnO(111) structure would rather result in a $c(8\times2)$ coincidence lattice.
[44] H. Nishimura, T. Tashiro, T. Fujitani, and J. Nakamura, J. Vac. Sci. Technol. A **18**, 1460 (2000).
[45] J. Gustafson, A. Mikkelsen, M. Borg, E. Lundgren, L. Köhler, G. Kresse, M. Schmid, P. Varga, J. Yuhara, X. Torrelles, C. Quirós, and J. N. Andersen, Phys. Rev. Lett. **92**, 126102 (2004).
[46] J. Gustafson, A. Mikkelsen, M. Borg, J. N. Anderson, E. Lundgren, C. Klein, W. Hofer, M. Schmid, P. Varga, L. Köhler, G. Kresse, N. Kasper, A. Stierle, and H. Dosch, Phys. Rev. B **71**, 115442 (2005).
[47] Y. B. He, A. Stierle, W. X. Li, A. Farkas, N. Kasper, and H. Over, J. Phys. Chem. **112**, 11946 (2008).